

# NONLINEAR COLLECTIVE PROCESSES IN VERY DENSE PLASMAS

P. K. SHUKLA\* and B. ELIASSON

*Institut für Theoretische Physik IV, Fakultät für Physik und Astronomie,  
Ruhr-Universität Bochum,  
D-44780 Bochum, Germany*

*\* E-mail: ps@tp4.rub.de*

*www.tp4.rub.de*

D. SHAIKH

*Institute of Geophysics and Planetary Physics,  
University of California, Riverside, CA 92521, USA*

We present simulation studies of the formation and dynamics of dark solitons and vortices, and of nonlinear interactions between intense circularly polarized electromagnetic (CPEM) waves and electron plasma oscillations (EPOs) dense in quantum electron plasmas. The electron dynamics in the latter is governed by a pair of equations comprising the nonlinear Schrödinger and Poisson system of equations, which conserves electrons and their momentum and energy. Nonlinear fluid simulations are carried out to investigate the properties of fully developed two-dimensional (2D) electron fluid turbulence in a dense Fermi (quantum) plasma. We report several distinguished features that have resulted from our 2D computer simulations of the nonlinear equations which govern the dynamics of nonlinearly interacting electron plasma oscillations (EPOs) in the Fermi plasma. We find that a 2D quantum electron plasma exhibits dual cascades, in which the electron number density cascades towards smaller turbulent scales, while the electrostatic potential forms larger scale eddies. The characteristic turbulent spectrum associated with the nonlinear electron plasma oscillations determined critically by quantum tunneling effect. The turbulent transport corresponding to the large-scale potential distribution is predominant in comparison with the small-scale electron number density variation, a result that is consistent with the classical diffusion theory. The dynamics of the CPEM waves is also governed by a nonlinear Schrödinger equation, which is nonlinearly coupled with the nonlinear Schrödinger equation of the EPOs via the relativistic ponderomotive force, the relativistic electron mass increase in the CPEM field, and the electron density fluctuations. The present governing equations in one spatial dimension admit stationary solutions in the form of a dark envelope soliton. The dynamics of the latter reveals its robustness. Furthermore, we numerically demonstrate the existence of cylindrically

symmetric two-dimensional quantum electron vortices, which survive during collisions. The nonlinear equations admit the modulational instability of an intense CPEM pump wave against EPOs, leading to the formation and trapping of localized CPEM wave pipes in the electron density hole that is associated with a positive potential distribution in our dense plasma.

## 1. Introduction

About forty five years ago, Pines<sup>1</sup> had laid down foundations for quantum plasma physics through his studies of the properties of electron plasma oscillations (EPOs) in a dense Fermi plasma. The high-density, low-temperature quantum Fermi plasma is significantly different from the low-density, high-temperature “classical plasma” obeying the Maxwell-Boltzmann distribution. In a very dense quantum plasma, there are new equations of state<sup>2-4</sup> associated with the Fermi-Dirac plasma particle distribution function and there are new quantum forces involving the quantum Bohm potential<sup>5</sup> and the electron-1/2 spin effect<sup>6</sup> due to magnetization. It should be noted that very dense quantum plasmas exist in intense laser-solid density plasma interaction experiments,<sup>7-10</sup> in laser-based inertial fusion,<sup>11</sup> in astrophysical and cosmological environments,<sup>12-15</sup> and in quantum diodes.<sup>16-18</sup>

During the last decade, there has been a growing interest in investigating new aspects of dense quantum plasmas by developing the quantum hydrodynamic (QHD) equations<sup>5</sup> by incorporating the quantum force associated with the Bohm potential.<sup>5</sup> The the Wigner-Poisson (WP) model<sup>19,20</sup> has been used to derive a set of quantum hydrodynamic (QHD) equations<sup>2,3</sup> for a dense electron plasma. The QHD equations include the continuity, momentum and Poisson equations. The quantum nature<sup>2</sup> appears in the electron momentum equation through the pressure term, which requires the knowledge of the Wigner distribution for a quantum mixture of electron wave functions, each characterized by an occupation probability. The quantum part of the electron pressure is represented as a quantum force<sup>2,5</sup>  $-\nabla\phi_B$ , where  $\phi_B = -(\hbar^2/2m_e\sqrt{n_e})\nabla^2\sqrt{n_e}$ ,  $\hbar$  is the Planck constant divided by  $2\pi$ ,  $m_e$  is the electron mass, and  $n_e$  is the electron number density. Defining the effective wave function  $\psi = \sqrt{n_e(\mathbf{r}, t)} \exp[iS(\mathbf{r}, t)/\hbar]$ , where  $\nabla S(\mathbf{r}, t) = m_e \mathbf{u}_e(\mathbf{r}, t)$  and  $\mathbf{u}_e(\mathbf{r}, t)$  is the electron velocity, the electron momentum equation can be represented as an effective nonlinear Schrödinger (NLS) equation,<sup>2-4</sup> in which there appears a coupling between the wave function and the electrostatic potential associated with the EPOs. The electrostatic potential is determined from the Poisson equation. We thus have the coupled NLS and Poisson equations, which govern the dynamics of nonlinearly interacting EPOs in a dense quantum plasmas. This mean-

field model of Ref.<sup>2,3</sup> is valid to the lowest order in the correlation parameter, and it neglects correlations between electrons. The QHD equations is useful for deriving the Child-Langmuir law in the quantum regime<sup>17,18</sup> and for studying numerous collective effects<sup>2-4,21-24</sup> involving different quantum forces (e.g. due to the Bohm potential<sup>5</sup> and the pressure law<sup>2,3</sup> for the Fermi plasma, as well as the potential energy of the electron-1/2 spin magnetic moment in a magnetic field<sup>44</sup>). In dense plasmas, quantum mechanical effects (e.g. tunnelling) are important since the de Broglie length of the charge carriers (e.g. electrons and holes/positrons) is comparable to the dimensions of the system. Studies of collective interactions in dense quantum plasmas are relevant for the next generation intense laser-solid density plasma experiments,<sup>8,10,25</sup> for superdense astrophysical bodies<sup>12,14,15,26</sup> (e.g. the interior of white dwarfs and neutron stars), as well as for micro and nano-scale objects (e.g. quantum diodes,<sup>17,18</sup> quantum dots and nanowires,<sup>27</sup> nano-photonics,<sup>28,29</sup> ultra-small electronic devices<sup>30</sup>) and micro-plasmas.<sup>31</sup> Quantum transport models similar to the QHD plasma model has also been used in superfluidity<sup>32</sup> and superconductivity,<sup>33</sup> as well as the study of metal clusters and nanoparticles, where they are referred to as nonstationary Thomas-Fermi models.<sup>34</sup> The density functional theory<sup>35-37</sup> incorporates electron-electron correlations, which are neglected in the present paper.

It has been recently recognized<sup>25,38,39</sup> that quantum mechanical effects play an important role in intense laser-solid density plasma interaction experiments. In the latter, there are nonlinearities<sup>40</sup> associated with the electron mass increase in the electromagnetic (EM) fields and the modification of the electron number density by the relativistic ponderomotive force. Relativistic nonlinear effects in a classical plasma is very important, because they provide the possibility of the compression and localization of intense electromagnetic waves. In this Letter, we consider nonlinear interactions between intense CPEM waves and EPOs in dense quantum plasmas, which are relevant for a variety of applications in laboratories.<sup>9,10</sup>

In this paper, we investigate, by means of computer simulations, the formation and dynamics of dark/gray envelope solitons and vortices in quantum electron plasmas with fixed ion background. The results are relevant for the transport of information at quantum scales in micro-plasmas as well as in micro-mechanical systems and microelectronics. For our purposes, we shall use an effective Schrödinger-Poisson model,<sup>2,21-24</sup> which was developed by employing the Wigner-Poisson phase space formalism on the Vlasov equation coupled with the Poisson equation for the electric potential. Such

a model was originally derived by Hartree in the context of atomic physics for studying the self-consistent effect of atomic electrons on the Coulomb potential of the nucleus. The properties of 2D electron fluid turbulence and associated electron transport in quantum plasmas are investigated numerically by simulations. We find that the nonlinear coupling between the EPOs of different scale sizes gives rise to small-scale electron density structures, while the electrostatic potential cascades towards large-scales. Finally, we present theoretical and simulation studies of the CPEM wave modulational instability against EPOs, as well as the trapping of localized CPEM waves into a quantum electron hole in very dense quantum plasmas, which may be relevant for the next generation intense laser-plasma interaction experiments.

## 2. Dark solitons and vortices in a dense quantum plasma

In this section, we discuss the nonlinear properties and dynamics of dark solitons and vortices in a quantum plasma.<sup>4</sup> Generalizing the one-dimensional Schrödinger-Poisson system of equations<sup>2</sup> to multi-space dimensions, we have

$$i\frac{\partial\Psi}{\partial t} + A\nabla^2\Psi + \varphi\Psi - |\Psi|^4\Psi = 0, \quad (1)$$

and

$$\nabla^2\varphi = |\Psi|^2 - 1, \quad (2)$$

where the wave function  $\Psi$  is normalized by  $\sqrt{n_0}$ , the electrostatic potential  $\varphi$  by  $k_B T_F/e$ , the time  $t$  by  $\hbar K_B T_F$  and the space  $\mathbf{r}$  by  $\lambda_D$ . We have introduced the notations  $\lambda_D = (k_B T_F/4\pi n_0 e^2)^{1/2}$  and  $A = \Gamma_Q/2$ , where the quantum coupling parameter  $\Gamma_Q = 4\pi e^2 m/\hbar n_0^{1/3}$  can be both smaller and larger than unity for typical metallic electrons.<sup>2</sup> Here  $n_0$  is the equilibrium electron particle density,  $k_B T_F \simeq \hbar n_0^{2/3}/m_e$  is the Fermi temperature,  $m_e$  is the electron mass,  $e$  is the magnitude of the electron charge,  $k_B$  is Boltzmann's constant, and  $\hbar$  is the Planck constant divided by  $2\pi$ . Strictly speaking, the nonlinearity  $|\Psi|^4$  in the last term in the left-hand side of Eq. (1) was derived for the one-dimensional model<sup>2</sup> and takes the form  $|\Psi|^{4/D}$  in  $D$  dimensions. However, our numerical investigations of the profiles of dark solitons and vortices have shown very small differences if we use  $D = 2$  (for two dimensions) instead of  $D = 1$ ; henceforth, we will keep Eqs. (1) and (2) in the present form. The system (1) and (2) is supplemented by the Maxwell equation

$$\partial\mathbf{E}/\partial t = iA(\Psi\nabla\Psi^* - \Psi^*\nabla\Psi), \quad (3)$$

where the electric field  $\mathbf{E} = -\nabla\varphi$ . The system of equations (1)–(3) conserves the number of electrons  $N = \int |\Psi| d^3x$ , the electron momentum  $\mathbf{P} = -i \int \Psi^* \nabla \Psi d^3x$ , the electron angular momentum  $\mathbf{L} = -i \int \Psi^* \mathbf{r} \times \nabla \Psi d^3x$ , and the total energy  $\mathcal{E} = \int (-\Psi^* A \nabla^2 \Psi + |\nabla\varphi|^2/2 + |\Psi|^6/3) d^3x$ . We note that one-dimensional version of Eq. (1) without the  $\varphi$ -term has also been used to describe the behaviour of a Bose-Einstein condensate.<sup>41</sup>

Let us first consider a quasi-stationary, one-dimensional structure moving with a constant speed  $v_0$ , and make the ansatz  $\Psi = W(\xi) \exp(iKx - i\Omega t)$ , where  $W$  is a complex-valued function of the argument  $\xi = x - v_0 t$ , and  $K$  and  $\Omega$  are a constant wavenumber and frequency shift, respectively. By the choice  $K = v_0/2A$ , we can then write the coupled system of equations as

$$\frac{d^2 W}{d\xi^2} + \lambda W + \frac{\varphi W}{A} - \frac{|W|^4 W}{A} = 0, \quad (4)$$

and

$$\frac{d^2 \varphi}{d\xi^2} = |W|^2 - 1, \quad (5)$$

where  $\lambda = \Omega/A - v_0^2/4A^2$  is an eigenvalue of the system. From the boundary conditions  $|W| = 1$  and  $\varphi = 0$  at  $|\xi| = \infty$ , we determine  $\lambda = 1/A$  and  $\Omega = 1 + v_0^2/4A$ . The system of Eqs. (4) and (5) supports a first integral in the form

$$H = A \left| \frac{dW}{d\xi} \right|^2 - \frac{1}{2} \left( \frac{d\varphi}{d\xi} \right)^2 + |W|^2 - \frac{|W|^6}{3} + \varphi |W|^2 - \varphi - \frac{2}{3} = 0, \quad (6)$$

where we have used the boundary conditions  $|W| = 1$  and  $\varphi = 0$  at  $|\xi| = \infty$ .

We have solved (4) and (5) numerically and have presented the results in Fig. 1. Here we have plotted the profiles of  $W^2$  and  $\varphi$  for a few values of  $A$ , where  $W$  was set to  $-1$  on the left boundary and to  $+1$  on the right boundary, i.e. the phase shift is 180 degrees between the two boundaries. We see that we have solutions in the form of a dark soliton, with a localized depletion of the electron density  $N_e = |W|^2$ , and where  $W$  has different sign on different sides of the solitary structure. The local depletion of the electron density is associated with a positive potential. Larger values of the parameter  $A$  give rise to larger-amplitude and wider dark solitons. Unlike a dark soliton associated with usual cubic Schrödinger equation in which the group dispersion and the nonlinearity coefficient have opposite sign, the

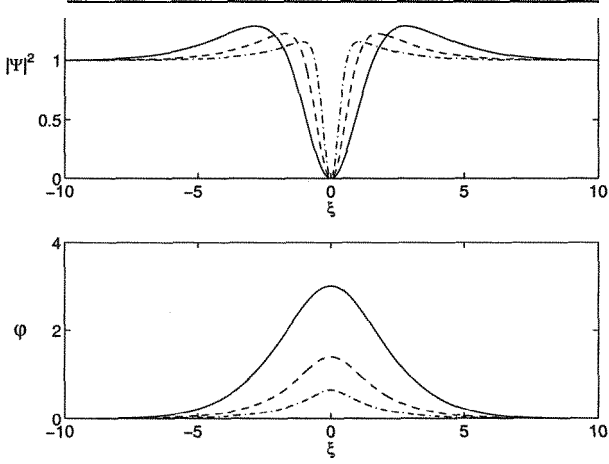


Fig. 1. The electron density  $|\Psi|^2$  (the upper panel) and electrostatic potential  $\varphi$  (the lower panel) associated with a dark soliton supported by the system of equations (4) and (5), for  $A = 5$  (solid lines),  $A = 1$  (dashed lines), and  $A = 0.2$  (dash-dotted line). After Ref. 4.

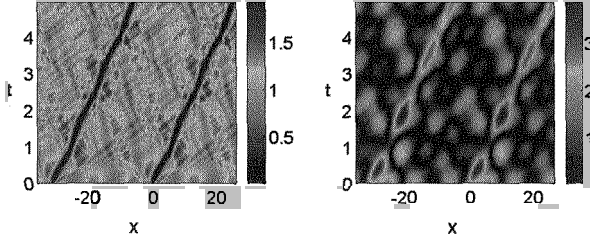


Fig. 2. The time-development of the electron density  $|\Psi|^2$  (left-hand panel) and electrostatic potential  $\varphi$  (the right-hand panel), obtained from a simulation of the system of equations (1) and (2). The initial condition is  $\Psi = 0.18 + \tanh[20 \sin(x/10)] \exp(iKx)$ , with  $K = v_0/2A$ ,  $A = 5$  and  $v_0 = 5$ . After Ref. 4.

modulus of the wave function in the present work has localized maxima on both sides of the density depletion. If the boundary conditions are shifted below 180 degrees (i.e. by a complex number), we have a “grey soliton” which is characterized by a non-zero density at the center of the soliton. In order to assess the dynamics and stability of the dark soliton, we have solved the time-dependent system of Eqs. (1) and (2) numerically, and have displayed the result in Fig. 2. The initial condition is  $\Psi = 0.18 + \tanh[20 \sin(x/10)] \exp(iKx)$ , where  $K = v_0/2A$ ,  $A = 5$  and  $v_0 = 5$ . We

clearly see oscillations and wave turbulence in the time-dependent solution presented in Fig. 2. Two very clear and long-lived dark solitons are visible, associated with a positive potential of  $\varphi \approx 3$ , which is consistent with the quasi-stationary solution of Fig. 1 for  $A = 5$ . Hence, the dark solitons seem to be robust structures that can withstand perturbations and turbulence during a considerable time.

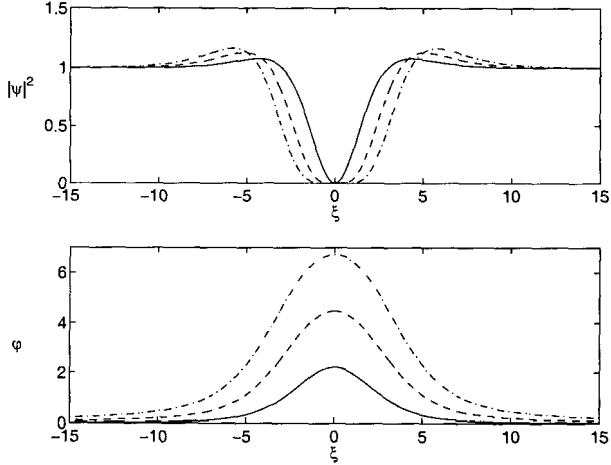


Fig. 3. The electron density  $|\Psi|^2$  (upper panel) and electrostatic potential  $\varphi$  (lower panel) associated with a two-dimensional vortex supported by the system (7) and (8), for the charge states  $n = 1$  (solid lines),  $n = 2$  (dashed lines) and  $n = 3$  (dash-dotted lines). We used  $A = 5$  in all cases. After Ref. 4.

We next consider two-dimensional vortex structures of the form  $\Psi = \psi(r) \exp(in\theta - i\Omega t)$ , where  $r$  and  $\theta$  are the polar coordinates defined via  $x = r \cos(\theta)$  and  $y = r \sin(\theta)$ ,  $\Omega$  is a constant frequency shift, and  $n = 0, \pm 1, \pm 2, \dots$  for different excited states (charge states). With this, we can write Eqs. (1) and (2) in the form

$$\Omega\psi + A \left( \frac{d^2}{dr^2} + \frac{1}{r} \frac{d}{dr} - \frac{n^2}{r^2} \right) \psi + \varphi\psi - |\psi|^4\psi = 0, \quad (7)$$

and

$$\left( \frac{d^2}{dr^2} + \frac{1}{r} \frac{d}{dr} \right) \varphi = |\psi|^2 - 1, \quad (8)$$

respectively, where the boundary conditions  $\psi = 1$  and  $\varphi = d\psi/dr = 0$  at  $r = \infty$  determine  $\Omega = 1$ . Different signs of  $n$  describe different rotation

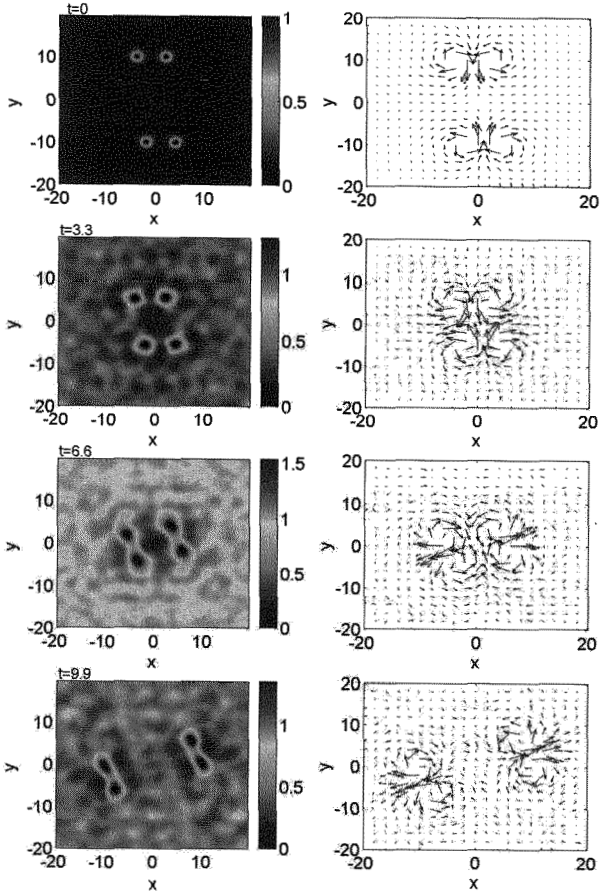


Fig. 4. The electron density  $|\Psi|^2$  (left panel) and an arrow plot of the electron current  $i(\Psi\nabla\Psi^* - \Psi^*\nabla\Psi)$  (right panel) associated with singly charged ( $n = 1$ ) two-dimensional vortices, obtained from a simulation of the time-dependent system of equations (1) and (2), at times  $t = 0$ ,  $t = 3.3$ ,  $t = 6.6$  and  $t = 9.9$  (upper to lower panels). We used  $A = 5$ . The singly charged vortices form pairs and keep their identities. After Ref. 4.

directions of the vortex. For  $n \neq 0$ , we must have  $\psi = 0$  at  $r = 0$ , and from symmetry considerations we have  $d\varphi/dr = 0$  at  $r = 0$ . In Fig. 3, we display numerical solutions of Eqs. (7) and (8) for different charge states  $n$  and for  $A = 5$ . We see that the vortex is characterized by a complete depletion of the electron density at the core of the vortex, and is associated with a positive electrostatic potential. In order to assess the stability of the vortices, we have numerically solved the time-dependent system of Eqs. (1)

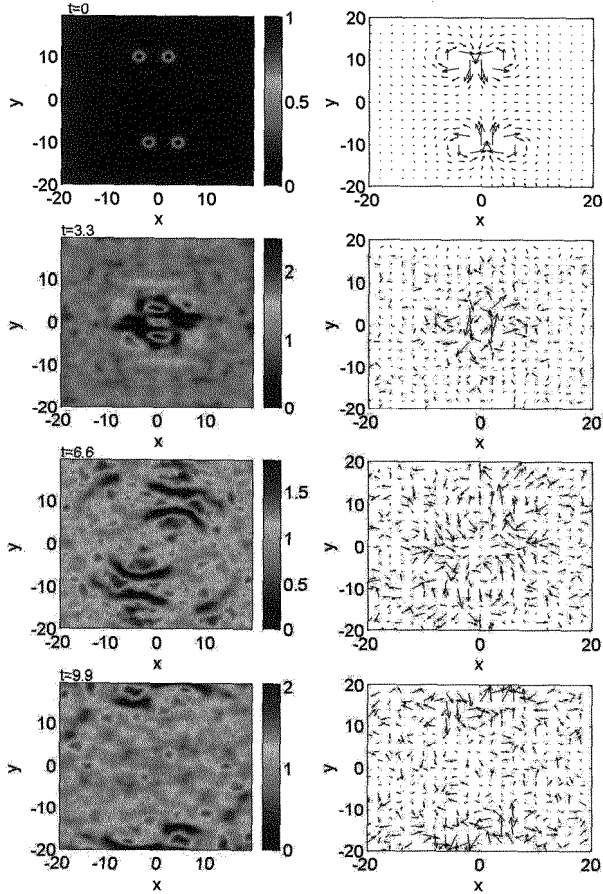


Fig. 5. The electron density  $|\Psi|^2$  (left panel) and an arrow plot of the electron current  $i(\Psi \nabla \Psi^* - \Psi^* \nabla \Psi)$  (right panel) associated with double charged ( $n = 2$ ) two-dimensional vortices, obtained from a simulation of the time-dependent system of Eqs. (1) and (2), at times  $t = 0$ ,  $t = 3.3$ ,  $t = 6.6$  and  $t = 9.9$  (upper to lower panels). We used  $A = 5$ . The doubly charged vortices dissolve into nonlinear structures and wave turbulence. After Ref. 4.

and (2) in two-space dimensions for singly charged vortices and presented our results in Fig. 4. We have placed four vortex-like structures at some distance from each other, by the initial condition  $\Psi = f_1 f_2 f_3 f_4$ , where  $f_j = \tanh[\sqrt{(x - x_j)^2 + (y - y_j)^2}] \exp[+in \arg(x - x_j, y - y_j)]$ . Here  $(x_1, y_1) = (-4, 10)$ ,  $(x_2, y_2) = (2, 10)$ ,  $(x_3, y_3) = (-2, -10)$ , and  $(x_4, y_4) = (4, -10)$ . The function  $\arg(x, y)$  denotes the angle between the  $x$  axis and the point

$(x, y)$ , and it takes values between  $-\pi$  and  $\pi$ . The initial conditions are such that the vortices are organized in two vortex pairs, as seen in the upper panels of Fig. 4. The vortices in the pairs have opposite polarity on the rotation, as seen in the electron fluid rotation direction in the upper right panel. The time-development of the system exhibits that the “partners” in the vortex pairs attract each other and propagate together with a constant velocity. When the two vortex pairs collide and interact (see the second and third pairs of panels in Fig. 4), the vortices keep their identities and change partners in a manner of asymptotic freedom, resulting into two new vortex pairs which propagate obliquely to the original propagation direction. For vortices that are multiply charged ( $|n| > 1$ ), we have a breakup of the vortices and the formation of quasi one-dimensional dark solitons and pairs of vortices with single charge states. One such example is shown in Fig. 5, where we have simulated the system of Eqs. (1) and (2), with the same initial condition as the one in Fig. 4, except that we here have taken  $n = 2$  to make the vortices doubly charged. The second row of panels in Fig. 5 reveals that the vortex pairs keep their identities for some time, while a quasi one-dimensional density cavity is formed between the two vortex pairs. At a later stage, the four vortices dissolve into complicated nonlinear structures and wave turbulence. Hence, the nonlinear dynamics is very different between singly and multiply charged solitons, where only singly charged vortices are long-lived and keep their identities. This is in line with previous results on the nonlinear Schrödinger equation, where it was noted that vortices with higher charge states are unstable.<sup>42</sup> In the numerical simulations of Eqs. (1) and (2), we used a pseudo-spectral method to approximate the  $x$  and  $y$  derivatives and a fourth-order Runge-Kutta scheme for the time-stepping. The numerical simulations confirmed the conservation laws of the electron number, momentum and energy up to the accuracy of the numerical scheme. The numerical solutions of the time-independent systems (4)–(5) and (7)–(8) were obtained by using the Newton method, where the  $\xi$  derivatives were approximated with a second-order centered difference scheme with appropriate boundary conditions on  $\Psi$  and  $\varphi$ .

### 3. Turbulence in quantum plasmas

In this Section, we use the coupled NLS and Poisson equations for investigating, by means of computer simulations, the properties of 2D electron fluid turbulence and associated electron transport in quantum plasmas.<sup>43</sup> We find that the nonlinear coupling between the EPOs of different scale sizes gives rise to small-scale electron density structures, while the elec-

trostatic potential cascades towards large-scales. The total energy associated with our quantum electron plasma turbulence, nonetheless, processes a characteristic spectrum, which is a *non-* Kolmogorov-like. The electron diffusion caused by the electron fluid turbulence is consistent with the dynamical evolution of turbulent mode structures.

For our 2D turbulence studies, we use the nonlinear Schrödinger-Poisson equations<sup>2,4</sup>

$$i\sqrt{2H}\frac{\partial\Psi}{\partial t} + H\nabla^2\Psi + \varphi\Psi - |\Psi|^2\Psi = 0, \quad (9)$$

and

$$\nabla^2\varphi = |\Psi|^2 - 1, \quad (10)$$

which are valid at zero electron temperature for the Fermi-Dirac equilibrium distribution, and which govern the dynamics of nonlinearly interacting EPOs of different wavelengths. In Eqs. (9) and (10) the wave function  $\Psi$  is normalized by  $\sqrt{n_0}$ , the electrostatic potential  $\varphi$  by  $k_B T_F/e$ , the time  $t$  by the electron plasma period  $\omega_{pe}^{-1}$ , and the space  $\mathbf{r}$  by the Fermi Debye radius  $\lambda_D$ . We have introduced the notations  $\lambda_D = (k_B T_F/4\pi n_0 e^2)^{1/2} \equiv V_F/\omega_{pe}$  and  $\sqrt{H} = \hbar\omega_{pe}/\sqrt{2}k_B T_F$ , where the Fermi electron temperature  $k_B T_F = (\hbar^2/2m_e)(3\pi^2)^{1/3}n_0^{2/3}$ ,  $e$  is magnitude of the electron charge, and  $\omega_{pe} = (4\pi n_0 e^2/m_e)^{1/2}$  is the electron plasma frequency. The origin of the various terms in Eq. (9) is obvious. The first term is due to the electron inertia, the  $H$ -term in (9) is associated from the quantum tunneling involving the Bohm potential,  $\varphi\Psi$  comes from the nonlinear coupling between the scalar potential (due to the space charge electric field) and the electron wave function, and the cubic nonlinear term is the contribution of the electron pressure<sup>2</sup> for the Fermi plasma that has a quantum statistical equation of state.

Equations (9) and (10) admit a set of conservation laws,<sup>44</sup> including the number of electrons  $N = \int \Psi^2 dx dy$ , the electron momentum  $\mathbf{P} = -i \int \Psi^* \nabla \Psi dx dy$ , the electron angular momentum  $\mathbf{L} = -i \int \Psi^* \mathbf{r} \times \nabla \Psi dx dy$ , and the total energy  $\mathcal{E} = \int [-\Psi^* H \nabla^2 \Psi + |\nabla \varphi|^2/2 + |\Psi|^3/2] dx dy$ . In obtaining the total energy  $\mathcal{E}$ , we have used the relation  $\partial \mathcal{E}/\partial t = iH(\Psi \nabla \Psi^* - \Psi^* \nabla \Psi)$ , where the electric field  $\mathbf{E} = -\nabla \varphi$ . The conservations laws are used to maintain the accuracy of the numerical integration of Eqs. (9) and (10), which hold for quantum electron-ion plasmas with fixed ion background. The assumption of immobile ions is valid, since the EPOs (given by the dispersion relation<sup>2,3</sup>  $\omega^2 = \omega_{pe}^2 + k^2 V_F^2 + \hbar^2 k^4/4m_e^2$ ) occur on the electron plasma period, which is much shorter than the ion plasma period  $\omega_{pi}^{-1}$ . Here

$\omega$  and  $k$  are the frequency and the wave-number, respectively. The ion dynamics, which may become important in the nonlinear phase on a longer timescale (say of the order of  $\omega_{pi}^{-1}$ ), in our investigation can easily be incorporated by replacing 1 in Eq. (10) by  $n_i$ , where the normalized (by  $n_0$ ) ion density  $n_i$  is determined from  $d_t n_i + n_i \nabla \cdot \mathbf{u}_i = 0$  and  $d_t \mathbf{u}_i = -C_s^2 \nabla \varphi$ , where  $d_t = (\partial/\partial t) + \mathbf{u}_i \cdot \nabla$ ,  $\mathbf{u}_i$  is the ion velocity,  $C_s = (T_F/m_i)^{1/2}$  is the ion sound speed, and  $m_i$  is the ion mass.

The nonlinear mode coupling interaction studies are performed to investigate the multi-scale evolution of a decaying 2D electron fluid turbulence, which is described by Eqs. (9) and (10). All the fluctuations are initialized isotropically (no mean fields are assumed) with random phases and amplitudes in Fourier space, and evolved further by the integration of Eqs. (9) and (10), using a fully de-aliased pseudospectral numerical scheme<sup>45</sup> based on the Fourier spectral methods. The spatial discretization in our 2D simulations uses a discrete Fourier representation of turbulent fluctuations. The numerical algorithm employed here conserves energy in terms of the dynamical fluid variables and not due to a separate energy equation written in a conservative form. The evolution variables use periodic boundary conditions. The initial isotropic turbulent spectrum was chosen close to  $k^{-2}$ , with random phases in all three directions. The choice of such (or even a flatter than  $-2$ ) spectrum treats the turbulent fluctuations on an equal footing and avoids any influence on the dynamical evolution that may be due to the initial spectral non-symmetry. The equations are advanced in time using a second-order predictor-corrector scheme. The code is made stable by a proper de-aliasing of spurious Fourier modes, and by choosing a relatively small time step in the simulations. Our code is massively parallelized using Message Passing Interface (MPI) libraries to facilitate higher resolution in a 2D computational box, with a resolution of  $512^2$  grid points.

We study the properties of 2D fluid turbulence, composed of nonlinearly interacting EPOs, for two specific physical systems. These are the dense plasmas in the next generation laser-based plasma compression (LBPC) schemes<sup>10</sup> as well as in superdense astrophysical objects<sup>14,15,26</sup> (e.g. white dwarfs). It is expected that in LBPC schemes, the electron number density may reach  $10^{27} \text{ cm}^{-3}$  and beyond. Hence, we have  $\omega_{pe} = 1.76 \times 10^{18} \text{ s}^{-1}$ ,  $k_B T_F = 1.7 \times 10^{-9} \text{ erg}$ ,  $\hbar \omega_{pe} = 1.7 \times 10^{-9} \text{ erg}$ , and  $H = 1$ . The Fermi Debye length  $\lambda_D = 0.1 \text{ \AA}$ . On the other hand, in the interior of white dwarfs, we typically have<sup>46</sup>  $n_0 \sim 10^{30} \text{ cm}^{-3}$  (such values are also common in dense neutron stars and supernovae), yielding  $\omega_{pe} = 5.64 \times 10^{19} \text{ s}^{-1}$ ,  $k_B T_F = 1.7 \times 10^{-7} \text{ erg}$ ,  $\hbar \omega_{pe} = 5.64 \times 10^{-8} \text{ erg}$ ,  $H \approx 0.3$ , and  $\lambda_D = 0.025 \text{ \AA}$ .

The numerical solutions of Eqs. (9) and (10) for  $H = 1$  and  $H = 0.025$  (corresponding to  $n_0 = 10^{27} \text{ cm}^{-3}$  and  $n_0 = 10^{30} \text{ cm}^{-3}$ , respectively) are displayed in Figs. 6 and 7, respectively, which are the electron number density and electrostatic (ES) potential distributions in the  $(x, y)$ -plane.

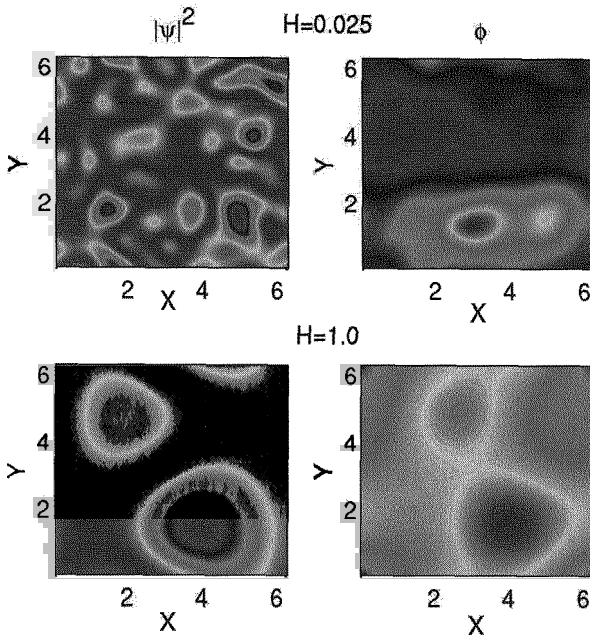


Fig. 6. Small scale fluctuations in the electron density resulted from a steady turbulence simulations of our 2D electron plasma. Forward cascades are responsible for the generation of small-scale fluctuations. Large scale structures are present in the electrostatic potential, essentially resulting from an inverse cascade. The 2D electron fluid turbulence interestingly relaxes towards an Iroshnikov-Kraichnan (IK) type  $k^{-3/2}$  spectrum in a dense plasma for  $H = 1$  as shown in the next figure. After Ref. 43.

Figures 6 and 7 reveal that the electron density distribution has a tendency to generate smaller length-scale structures, while the ES potential cascades towards larger scales. The co-existence of the small and larger scale structures in turbulence is a ubiquitous feature of various 2D turbulence systems. For example, in 2D hydrodynamic turbulence, the incompressible fluid admits two invariants, namely the energy and the mean squared vorticity. The two invariants, under the action of an external forcing, cascade simultaneously in turbulence, thereby leading to a dual cascade phenomena. In these processes, the energy cascades towards longer length-scales, while

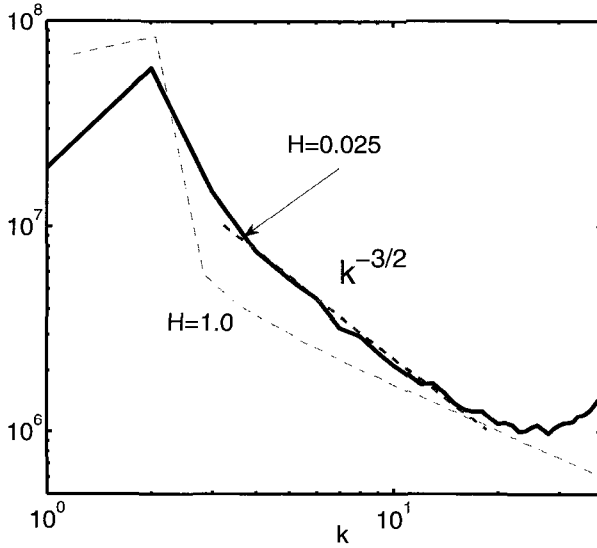


Fig. 7. The 2D electron fluid turbulence interestingly relaxes towards an Iroshnikov-Kraichnan (IK) type  $k^{-3/2}$  spectrum in a dense plasma for  $H = 1$ .  $H = 0.025$  results in a flat spectrum. After Ref. 43.

the fluid vorticity transfers spectral power towards shorter length-scales. Usually, a dual cascade is observed in a driven turbulence simulation, in which certain modes are excited externally through random turbulent forces in spectral space. The randomly excited Fourier modes transfer the spectral energy by conserving the constants of motion in  $k$ -space. On the other hand, in freely decaying turbulence, the energy contained in the large-scale eddies is transferred to the smaller scales, leading to a statistically stationary inertial regime associated with the forward cascades of one of the invariants. Decaying turbulence often leads to the formation of coherent structures as turbulence relaxes, thus making the nonlinear interactions rather inefficient when they are saturated. The power spectrum exhibits an interesting feature in our 2D electron plasma system, unlike the 2D hydrodynamic turbulence.<sup>47-49</sup> The spectral slope in the 2D quantum electron fluid turbulence is close to the Iroshnikov-Kraichnan power law<sup>50,51</sup>  $k^{-3/2}$ , rather than the usual Kolomogrov power law<sup>47</sup>  $k^{-5/3}$ . We further find that this scaling is not universal and is determined critically by the quantum tunneling effect. For instance, for a higher value of  $H=1.0$  the spectrum becomes more flat (see Fig 7). Physically, the flatness (or deviation from

the  $k^{-5/3}$ ), results from the short wavelength part of the EPOs spectrum which is controlled by the quantum tunneling effect associated with the Bohm potential. The peak in the energy spectrum can be attributed to the higher turbulent power residing in the EPO potential, which eventually leads to the generation of larger scale structures, as the total energy encompasses both the electrostatic potential and electron density components. In our dual cascade process, there is a delicate competition between the EPO dispersions caused by the statistical pressure law (giving the  $k^2 V_F^2$  term, which dominates at longer scales) and the quantum Bohm potential (giving the  $\hbar^2 k^4 / 4m_e^2$  term, which dominates at shorter scales with respect to a source). Furthermore, it is interesting to note that exponents other than  $k^{-5/3}$  have also been observed in numerical simulations<sup>52,53</sup> of the Charney and 2D incompressible Navier-Stokes equations.

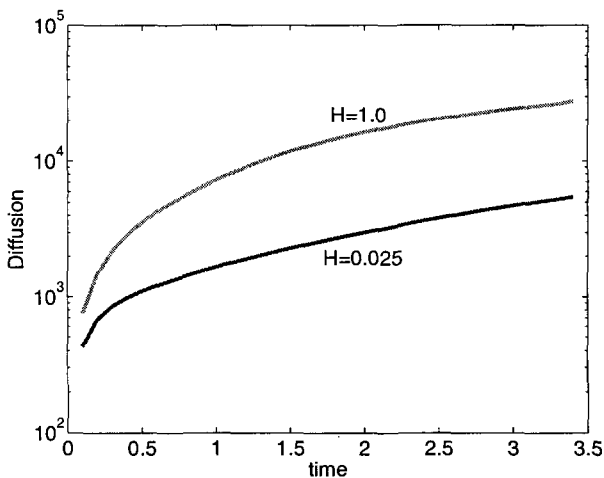


Fig. 8. Time evolution of an effective electron diffusion coefficient associated with the large-scale electrostatic potential and the small-scale electron density. Here a comparison between  $H = 1$  and  $H = 0.025$  is shown. After Ref. 43.

We finally estimate the electron diffusion coefficient in the presence of small and large scale turbulent EPOs in our quantum plasma. An effective electron diffusion coefficient caused by the momentum transfer can be calculated from  $D_{eff} = \int_0^\infty \langle \mathbf{P}(\mathbf{r}, t) \cdot \mathbf{P}(\mathbf{r}, t+t') \rangle dt'$ , where  $\mathbf{P}$  is electron momentum and the angular bracket denotes spatial averages and the ensemble averages are normalized to unit mass. Since the 2D structures are confined to a  $x-y$  plane, the effective electron diffusion coefficient,  $D_{eff}$ , essentially

relates the diffusion processes associated with random translational motions of the electrons in nonlinear plasmonic fields. We compute  $D_{eff}$  in our simulations, to measure the turbulent electron transport that is associated with the turbulent structures that we have reported herein. It is observed that the effective electron diffusion is lower when the field perturbations are Gaussian. On the other hand, the electron diffusion increases rapidly with the eventual formation of longer length-scale structures, as shown in Fig. 8. The electron diffusion due to large scale potential distributions in quantum plasmas dominates substantially, as depicted by the solid-curve in Fig. 8. Furthermore, in the steady-state, nonlinearly coupled EPOs form stationary structures, and  $D_{eff}$  saturates eventually. Thus, remarkably an enhanced electron diffusion results primarily due to the emergence of large-scale potential structures in our 2D quantum plasma.

#### 4. Interaction between intense electromagnetic waves and quantum plasma oscillations

In this section, we discuss the nonlinear interaction between intense electromagnetic radiation and quantum plasma oscillations.<sup>54</sup> We consider a one-dimensional geometry of an unmagnetized dense electron-ion plasma, in which immobile ions form the neutralizing background. Thus, we are investigating the phenomena on a timescale shorter than the ion plasma period. Our dense quantum plasma contains an intense circularly polarized electromagnetic (CPEM) plane wave that nonlinearly interacts with EPOs. The nonlinear interaction between intense CPEM waves and EPOs gives rise to an envelope of the CPEM vector potential  $\mathbf{A}_\perp = A_\perp(\hat{\mathbf{x}} + i\hat{\mathbf{y}})\exp(-i\omega_0 t + ik_0 z)$ , which obeys the nonlinear Schrödinger equation<sup>40</sup>

$$2i\Omega_0 \left( \frac{\partial}{\partial t} + V_g \frac{\partial}{\partial z} \right) A_\perp + \frac{\partial^2 A_\perp}{\partial z^2} - \left( \frac{|\psi|^2}{\gamma} - 1 \right) A_\perp = 0, \quad (11)$$

where the electron wave function  $\psi$  and the scalar potential are governed by, respectively,

$$iH_e \frac{\partial \psi}{\partial t} + \frac{H_e^2}{2} \frac{\partial^2 \psi}{\partial z^2} + (\phi - \gamma + 1)\psi = 0, \quad (12)$$

and

$$\frac{\partial^2 \phi}{\partial z^2} = |\psi|^2 - 1, \quad (13)$$

where  $\Omega_0 = \omega_0/\omega_{pe}$ ,  $V_g = v_g/c$ ,  $H_e = \hbar\omega_{pe}/mc^2$ ,  $v_g = k_0 c^2/\omega_0$  is the group velocity of the CPEM waves, and  $\gamma = (1 + |A_\perp|^2)^{1/2}$  is the relativistic

gamma factor due to the electron quiver velocity in the CPEM wave fields. Furthermore,  $\omega_0 = (k_0^2 c^2 + \omega_{pe}^2)^{1/2}$  is the CPEM wave frequency,  $k_0$  is the wavenumber,  $c$  is the speed of light in vacuum,  $\omega_{pe} = (4\pi n_0 e^2 / m)^{1/2}$  is the electron plasma frequency,  $e$  is the magnitude of the electron charge,  $n_0$  is the equilibrium electron number density, and  $m$  is the electron rest mass. In (11)–(13) the time and space variables are normalized by the inverse electron plasma frequency  $\omega_{pe}^{-1}$  and skin depth  $\lambda_e = c / \omega_{pe}$ , respectively, the scalar potential  $\phi$  by  $mc^2 / e$ , the vector potential  $A_\perp$  by  $mc^2 / e$ , and the electron wave function  $\psi(z, t)$  by  $n_0^{1/2}$ . The nonlinear coupling between intense CPEM waves and EPOs comes about due to the nonlinear current density, which is represented by the term  $|\psi|^2 A_\perp / \gamma$  in Eq. (11). The electron number density is defined as  $n_e = \psi \psi^* = |\psi|^2$ , where the asterisk denotes the complex conjugate. In Eq. (12),  $1 - \gamma$  is the relativistic ponderomotive potential,<sup>40</sup> which arises due to the cross-coupling between the CPEM wave-induced electron quiver velocity and the CPEM wave magnetic field. The second term in the left-hand side in (12) is associated with the quantum Bohm potential.<sup>5</sup>

It is well known<sup>55</sup> that a relativistically strong electromagnetic wave in a classical electron plasma is subjected to the Raman scattering and modulational instabilities. At quantum scales, these instabilities will be modified by the dispersive effects caused by the tunnelling of the electrons. In order to investigate the quantum mechanical effects on the relativistic parametric instabilities in a dense quantum plasma in the presence of a relativistically strong CPEM pump wave, we let  $\phi(z, t) = \phi_1(z, t)$ ,  $A_\perp(z, t) = [A_0 + A_1(z, t)] \exp(-i\alpha_0 t)$  and  $\psi(z, t) = [1 + \psi_1(z, t)] \exp(-i\beta_0 t)$ , where  $A_0$  is the large-amplitude CPEM pump and  $A_1$  is the small-amplitude fluctuations of the CPEM wave amplitude due to the nonlinear coupling between CPEM waves and EPOs, i.e.  $|A_1| \ll |A_0|$ , and  $\psi_1$  ( $\ll 1$ ) is the small-amplitude perturbations in the electron wave function. The constant frequency shifts, determined from Eqs. (11) and (12), are  $\alpha_0 = (1/\gamma_0 - 1)/(2\Omega_0)$  and  $\beta_0 = (1 - \gamma_0)/H_e$ , where  $\gamma_0 = (1 + |A_0|^2)^{1/2}$ . The first-order perturbations in the electromagnetic vector potential and the electron wave function are expanded into their respective sidebands as  $A_1(z, t) = A_+ \exp(iKz - i\Omega t) + A_- \exp(-iKz + i\Omega t)$  and  $\psi_1(z, t) = \psi_+ \exp(iKz - i\Omega t) + \psi_- \exp(-iKz + i\Omega t)$ , while the potential is expanded as  $\phi(z, t) = \hat{\phi} \exp(iKz - i\Omega t) + \hat{\phi}^* \exp(-iKz + i\Omega t)$ , where  $\Omega$  and  $K$  are the frequency and wave number of the electron plasma oscillations, respectively. Inserting the above mentioned Fourier ansatz into Eqs. (11)–(13), linearizing the resultant system of equations, and sorting into equations for

different Fourier modes, we obtain the nonlinear dispersion relation

$$1 - \left( \frac{1}{D_+} + \frac{1}{D_-} \right) \left( 1 + \frac{K^2}{D_L} \right) \frac{|A_0|^2}{2\gamma_0^3} = 0, \quad (14)$$

where  $D_{\pm} = \mp 2\Omega_0(\Omega - V_g K) + K^2$  and  $D_L = 1 + H_e^2 K^4/4 - \Omega^2$ . We note that  $D_L = 0$  yields the linear dispersion relation  $\Omega^2 = 1 + H_e^2 K^4/4$  for the EPOs in a dense quantum plasma.<sup>1</sup> For  $H_e \rightarrow 0$  we recover from (14) the nonlinear dispersion relation for relativistically large amplitude electromagnetic waves in a classical electron plasma.<sup>55</sup> The dispersion relation (14) governs the Raman backward and forward scattering instabilities, as well as the modulational instability. In the long wavelength limit  $V_g \ll 1$ ,  $\Omega_0 \approx 1$  we introduce the ansatz  $\Omega = i\Gamma$ , where the normalized (by  $\omega_{pe}$ ) growth rate  $\Gamma \ll 1$ , and obtain from Eq. (14) the growth rate  $\Gamma = (1/2)|K|\{(|A_0|^2/\gamma_0^3)[1 + K^2/(1 + H_e^2 K^4/4)] - K^2\}^{1/2}$  of the modulational instability. For  $|K| < 1$  and  $H_e < 1$ , the linear growth rate is only weakly depending on the quantum parameter  $H_e$ . However, possible nonlinear saturation of the modulational instability may lead to localized CPEM wave packets, which are trapped in a quantum electron hole. Such localized electromagnetic wavepackets would have length scales much shorter than those involved in the modulational instability process. Here quantum diffraction effects (associated with the quantum Bohm potential) become very important. In order to investigate the quantum diffraction effect on such localized electromagnetic pulses, we consider a steady state structure moving with a constant speed  $V_g$ . Inserting the ansatz  $A_{\perp} = W(\xi) \exp(-i\Omega t)$ ,  $\psi = P(\xi) \exp(ikx - i\omega t)$  and  $\phi = \phi(\xi)$  into Eqs. (11)–(13), where  $\xi = z - V_g t$ ,  $k = V_g/H_e$  and  $\omega = V_g^2/2H_e$ , and where  $W(\xi)$  and  $P(\xi)$  are real, we obtain from (11)–(13) the coupled system of equations

$$\frac{\partial^2 W}{\partial \xi^2} + \left( \lambda - \frac{P^2}{\gamma} + 1 \right) W = 0, \quad (15)$$

$$\frac{H_e^2}{2} \frac{\partial^2 P}{\partial \xi^2} + (\phi - \gamma + 1)P = 0, \quad (16)$$

where  $\gamma = (1 + W^2)^{1/2}$ , and

$$\frac{\partial^2 \phi}{\partial \xi^2} = P^2 - 1, \quad (17)$$

with the boundary conditions  $W = \Phi = 0$  and  $P^2 = 1$  at  $|\xi| = \infty$ . In Eq. (15),  $\lambda = 2\Omega_0\Omega$  represents a nonlinear frequency shift of the CPEM wave.

In the limit  $H_e \rightarrow 0$ , we have from (16)  $\phi = \gamma - 1$ , where  $P \neq 0$ , and we recover the classical (non-quantum) case of the relativistic solitary waves in a cold plasma.<sup>56</sup> We note that the system of equations (15)–(17) admits a Hamiltonian

$$Q_H = \frac{1}{2} \left( \frac{\partial W}{\partial \xi} \right)^2 + \frac{H_e^2}{2} \left( \frac{\partial P}{\partial \xi} \right)^2 - \frac{1}{2} \left( \frac{\partial \phi}{\partial \xi} \right)^2 + \frac{1}{2} (\lambda + 1) W^2 + P^2 - \gamma P^2 + \phi P^2 - \phi = 0, \quad (18)$$

where we have used the boundary conditions  $\partial/\partial\xi = 0$ ,  $W = \phi = 0$  and  $|P| = 1$  at  $|\xi| = \infty$ .

In order to assess the importance of our investigation, we now present numerical solutions of (8)–(13) and (15)–(17), ensuring that (18) is conserved. We chose parameters that are representative of the next generation laser-based plasma compression (LBPC) schemes.<sup>10,11</sup> The formula<sup>40</sup>  $eA_\perp/mc^2 = 6 \times 10^{-10} \lambda_s \sqrt{I}$  will determine the normalized vector potential, provided that the CPEM wavelength  $\lambda_s$  (in microns) and intensity  $I$  (in W/cm<sup>2</sup>) are known. It is expected that in LBPC schemes, the electron number density  $n_0$  may reach  $10^{27}$  cm<sup>-3</sup> and beyond, and the peak values of  $eA_\perp/mc^2$  may be in the range 1-2 (e.g. for focused EM pulses with  $\lambda_s \sim 0.15$  nm and  $I \sim 5 \times 10^{27}$  W/cm<sup>2</sup>). For  $\omega_{pe} = 1.76 \times 10^{18}$  s<sup>-1</sup>, we have  $\hbar\omega_{pe} = 1.76 \times 10^{-9}$  erg and  $H_e = 0.002$ , since  $mc^2 = 8.1 \times 10^{-7}$  erg. The electron skin depth  $\lambda_e \sim 1.7$  Å. On the other hand, a higher value of  $H_e = 0.007$  is achieved for  $\omega_{pe} = 5.64 \times 10^{18}$  s<sup>-1</sup>. Thus, our numerical solutions below, based on these two values of  $H_e$ , have focused on scenarios that are relevant for the next generation intense laser-solid density plasma interaction experiments.<sup>10</sup>

We first numerically solved Eqs. (15)–(17) for several values of  $H_e$ . Here, we solved the nonlinear boundary value problem with the boundary conditions  $W = \phi = 0$  and  $P = 1$  at the boundaries at  $\xi = \pm 10$ . We used centered second-order approximations for the second derivatives and solved the obtained nonlinear system of equations numerically by using the Newton method. The results are displayed in Figs. 9 and 10. We see that the solitary envelope pulse is composed of a single maximum of the localized vector potential  $W$  and a local depletion of the electron density  $P^2$ , and a localized positive potential  $\phi$  at the center of the solitary pulse. The latter has a continuous spectrum in  $\lambda$ , where larger values of negative  $\lambda$  are associated with larger amplitude solitary EM pulses. At the center of the solitary EM pulse, the electron density is partially depleted, as in panels a) of Fig. 9, and for larger amplitudes of the EM waves we have stronger depletion

of the electron density, as shown in panels b) and c) of Fig. 9. For cases where the electron density goes to almost zero in the classical case,<sup>56</sup> one important quantum effect is that the electrons can tunnel into the depleted region. This is seen in Fig. 10, where the electron density remains nonzero for the larger value of  $H_e$  in panels a), while the density shrinks to zero for the smaller value of  $H_e$  in panel b).

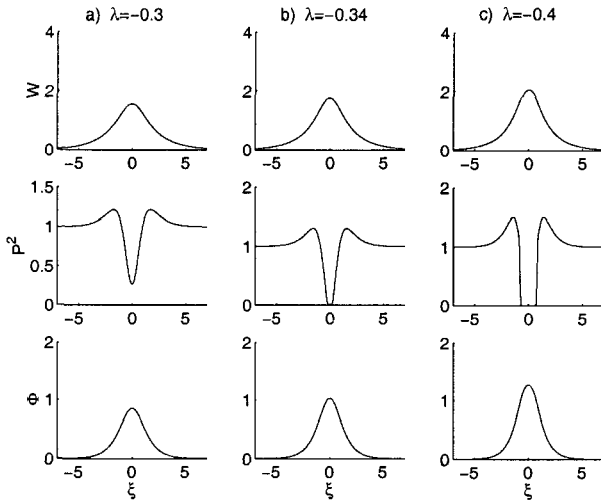


Fig. 9. The profiles of the CPEM vector potential  $A_{\perp}$ , the electron number density and the scalar potential (upper to lower rows of panels) for  $\lambda = -0.3$ ,  $\lambda = -0.34$  and  $\lambda = -0.4$ , with  $H_e = 0.002$ . After Ref. 54.

In order to investigate the quantum diffraction effects on the dynamics of localized CPEM wavepackets, we have solved the system of Eqs. (11)–(13) numerically. We considered the long-wavelength limit  $\omega_0 \approx 1$  and  $V_g \approx 0$ . In the initial conditions, we use an EM pump with a constant amplitude  $A_{\perp} = A_0 = 1$  and a uniform plasma density  $\psi = 1$ . A small amplitude noise (random numbers) of order  $10^{-2}$  is added to  $A_{\perp}$  to give a seed for any instability. The numerical results are displayed in Figs. 11 and 4 for  $H_e = 0.002$  and  $H_e = 0.007$ , respectively. In both cases, we see an initial linear growth phase and a wave collapse at  $t \approx 70$ , in which almost all the CPEM wave energy is contracted into a few well separated localized CPEM wave pipes. These are characterized by a large bell-shaped amplitude of the CPEM wave, an almost complete depletion of the electron number density at the center of the CPEM wavepacket, and a large-amplitude positive

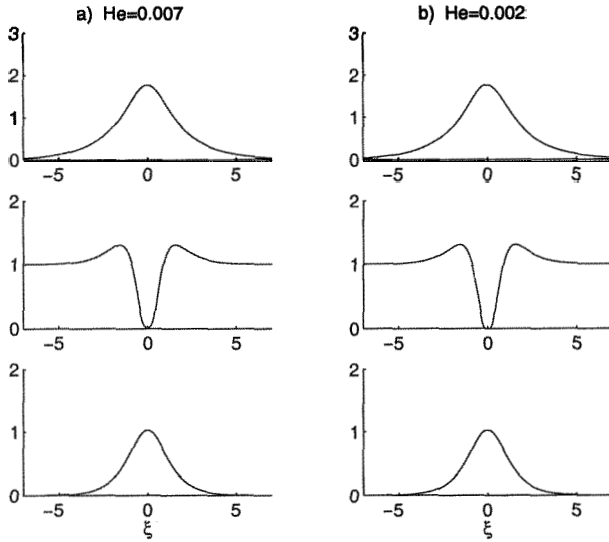


Fig. 10. The profiles of the CPEM vector potential  $A_{\perp}$ , the electron number density and the scalar potential (upper to lower rows of panels) for  $H_e = 0.007$  and  $H_e = 0.002$ , with  $\lambda = -0.34$ . After Ref. 54.

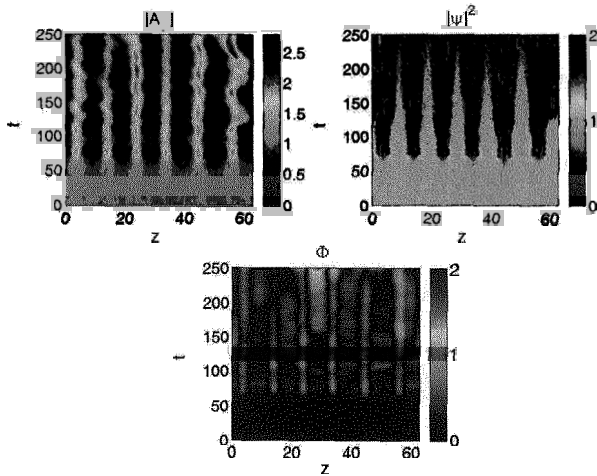


Fig. 11. The dynamics of the CPEM vector potential  $A_{\perp}$  and the electron number density  $|\psi|^2$  (upper panels) and of the electrostatic potential  $\Phi$  (lower panel) for  $H_e = 0.002$ . After Ref. 54.

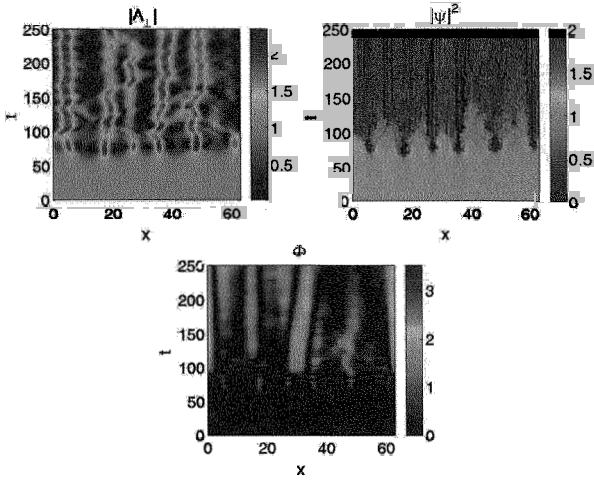


Fig. 12. The dynamics of the CPEM vector potential  $A_{\perp}$  and the electron number density  $|\psi|^2$  (upper panels) and the electrostatic potential  $\phi$  (lower panel) for  $H_e = 0.007$ . After Ref. 54.

electrostatic potential. Comparing Fig. 11 with Fig. 12, we see that there is a more complex dynamics in the interaction between the CPEM wavepackets for the larger  $H_e = 0.007$ , shown in Fig. 12, in comparison with  $H_e = 0.002$ , shown in Fig. 11, where the wavepackets are almost stationary when they are fully developed. We have here neglected the effects of the ion dynamics. The latter may be important for the development of expanding plasma bubbles (cavities) on longer timescales (e.g. the ion plasma period).<sup>57</sup>

## 5. Conclusions

In summary, we have demonstrated the existence of localized nonlinear structures in quantum electron plasmas. The electron dynamics in the latter is governed by a coupled nonlinear Schrödinger and Poisson system of equations, which admit a set of conserved quantities (the total number of electrons, the electron momentum, the electron angular momentum, and the electron energy). The latter were checked numerically. Quasi-stationary, localized structures in the form of one-dimensional dark solitons and two-dimensional vortices were found by solving the time-independent coupled system of equations numerically. These structures are associated with a local depletion of the electron density associated with positive electrostatic potential, and are parameterised by the quantum coupling parameter only.

In the two-dimensional geometry, we have a class of vortices of different excited states (charge states) associated with a complete depletion of the electron density and an associated positive potential. The numerical simulation of the time-dependent system of equations shows the formation of stable dark solitons in one-space dimension with an amplitude consistent with the one found from the time-independent solutions. In two-space dimensions, the dark solitons of the first excited state were found to be stable and the preferred nonlinear state was in the form of vortex pairs of vortices with different polarities. One-dimensional dark solitons and singly charge two-dimensional vortices are thus long-lived nonlinear structures, which can transport information at quantum scales in micro-mechanical systems and dense laboratory plasmas. We have presented computer simulation studies of 2D fluid turbulence in a dense quantum plasma. Our simulations, for the parameters that are representative of the next generation intense laser-solid density plasma experiments as well as of the superdense astrophysical bodies, reveal new features of the dual cascade in a fully developed 2D electron fluid turbulence. Specifically, we find that the power spectrum associated with nonlinearly interacting EPOs in quantum plasmas follow a non-Kolmogorov-like spectrum. The deviation from a Kolmogorov-like spectrum resulting from the flattening of the spectrum is mediated essentially by the nonlinear EPOs interactions in the inertial range (basically controlled by the electron plasma wave dispersion effect represented by  $\hbar^2 k^4 / 4m_e^2$ ), which impedes the spectral transfer of the turbulent power associated with the short scale Fourier modes. In the nonlinear regime, the inhibition of the spectral transfer is caused by short scale EPOs that are nonlinearly excited by the mode coupling of the EPOs in the forward cascade regime, which then grow, acquire nonlinear amplitudes, and eventually saturate in the nonlinear phase. We have also presented theoretical and computer simulation studies of nonlinearly interacting intense CPEM waves and EPOs in very dense quantum plasmas. The localized dark solitons, vortices, and CPEM wave structures, as discussed here, may be useful for information transfer as well as for electron acceleration in dense quantum plasmas.

## References

1. D. Pines, *J. Nucl. Energy: Part C: Plasma Phys.* **2**, 5 (1961).
2. G. Manfredi and F. Haas, *Phys. Rev. B* **64**, 075316 (2001).
3. G. Manfredi, *Fields Inst. Commun.* **46**, 263 (2005).
4. P. K. Shukla and B. Eliasson, *Phys. Rev. Lett.* **96** 245001 (2006).
5. C. L. Gardner and C. Ringhofer, *Phys. Rev. E* **53**, 157 (1996).

6. M. Marklund and G. Brodin, *Phys. Rev. Lett.* **98**, 025001 (2007).
7. S. X. Hu and C. H. Keitel, *Phys. Rev. Lett.* **83**, 4709 (1999).
8. Y. A. Salamin *et al.*, *Phys. Rep.* **427**, 41 (2006).
9. S. H. Glenzer *et al.*, *Phys. Rev. Lett.* **98**, 065002 (2007).
10. V. M. Malkin *et al.*, *Phys. Rev. E* **75**, 026404 (2007).
11. H. Azechi *et al.*, *Plasma Phys. Control. Fusion* **48**, B267 (2006).
12. M. Opher *et al.*, *Phys. Plasmas* **8**, 2454 (2001).
13. O. G. Benvenuto and M. A. De Vito, *Mon. Not. R. Astron. Soc.* **362**, 891 (2005).
14. G. Chabrier *et al.*, *J. Phys.: Condens. Matter* **14**, 9133 (2002).
15. G. Chabrier *et al.*, *J. Phys. A: Math. Gen.* **39**, 4411 (2006).
16. Y. Y. Lau *et al.*, *Phys. Rev. Lett.* **66**, 1446 (1991).
17. L. K. Ang *et al.*, *Phys. Rev. Lett.* **91**, 208303 (2003).
18. L. K. Ang and P. Zhang, *Phys. Rev. Lett.* **98**, 164802 (2007).
19. E. P. Wigner, *Phys. Rev.* **40**, 749 (1932).
20. M. Hillery *et al.*, *Phys. Rep.* **106**, 121 (1984).
21. F. Haas, G. Manfredi, and M. Feix, *Phys. Rev. E* **62**, 2763 (2000).
22. D. Anderson *et al.*, *Phys. Rev. E* **65**, 046417 (2002).
23. F. Haas, L. G. Garcia, J. Goedert, and G. Manfredi, *Phys. Plasmas* **10**, 3858 (2003).
24. F. Haas, *Phys. Plasmas* **12**, 062117 (2005).
25. G. Mourou *et al.*, *Rev. Mod. Phys.* **78**, 309 (2006).
26. A. K. Harding and D. Lai, *Rep. Prog. Phys.* **69**, 2631 (2006).
27. G. V. Shpatakovskaya, *J. Exp. Teor. Phys.* **102**, 466 (2006).
28. W. L. Barnes *et al.*, *Nature (London)* **424**, 824 (2003).
29. D. E. Chang *et al.*, *Phys. Rev. Lett.* **97**, 053002 (2006).
30. P. A. Markowich *et al.*, *Semiconductor Equations* (Springer, Berlin, 1990).
31. K. H. Becker, K. H. Schoenbach, and J. G. Eden, *J. Phys. D: Appl. Phys.* **39**, R55 (2006).
32. M. Loffredo and L. Morato, *Nuovo Cimento Soc. Ital. Fis. B* **108B**, 205 (1993).
33. R. Feynman, *Statistical Mechanics, A Set of of Lectures* (Benjamin, Reading, 1972).
34. A. Doms *et al.*, *Phys. Rev. Lett.* **80**, 5520 (1998).
35. P. Hohenberg and W. Kohn, *Phys. Rev.* **136**, B864 (1964).
36. W. Kohn and L. J. Sham, *Phys. Rev.* **140**, A1133 (1965).
37. L. Brey *et al.*, *Phys. Rev. B* **42**, 1240 (1990).
38. A. V. Andreev, *JETP Lett.* **72**, 238 (2000).
39. M. Marklund and P. K. Shukla, *Rev. Mod. Phys.* **78**, 591 (2006).
40. P. K. Shukla *et al.*, *Phys. Rep.* **138**, 1 (1986).
41. E. B. Kolomeisky *et al.*, *Phys. Rev. Lett.* **85**, 1146 (2000).
42. I. A. Ivonin, V. P. Pavlenko, and H. Persson, *Phys. Rev. E* **60**, 492 (1999).
43. D. Shaikh and P. K. Shukla, *Phys. Rev. Lett.* **99**, 125002 (2007).
44. M. Marklund and G. Brodin, *Phys. Rev. Lett.* **98**, 025001 (2007).
45. D. Gottlieb and S. A. Orszag, *Numerical Analysis of Spectral Methods* (SIAM, Philadelphia, 1977).

46. I. Iben Jr. and A. V. Tutukov, *Astrophys. J.* **282**, 615 (1984).
47. A. N. Kolmogorov, *C. R. Acad. Sci. USSR* **30**, 301 (1941).
48. M. Lesieur, *Turbulence in Fluids* (Kluwer, Dordrecht, 1990).
49. U. Frisch, *Turbulence* (Cambridge University Press, Cambridge, England, 1995).
50. P. Iroshnikov, *Sov. Astron.* **7**, 566 (1963).
51. R. H. Kraichnan, *Phys. Fluids* **8**, 1385 (1965).
52. V. D. Larichev and J. C. McWilliams, *Phys. Fluids A* **3** 938 (1991).
53. R. K. Scott, *Phys. Rev. E* **75**, 046301 (2007).
54. P. K. Shukla and B. Eliasson, *Phys. Rev. Lett.* **99**, 096401 (2007).
55. C. J. McKinstrie and R. Bingham, *Phys. Fluids B* **4**, 2626 (1992).
56. J. H. Marburger and R. F. Tooper, *Phys. Rev. Lett.* **35**, 1001 (1975).
57. M. Borghesi *et al.*, *Phys. Rev. Lett.* **88**, 135002 (2002).